



Article

Effect of Different Post-Processing Thermal Treatments on the Fracture Toughness and Tempering Resistance of Additively Manufactured H13 Hot-Work Tool Steel

Faraz Deirmina ¹, Sasan Amirabdollahian ^{2,3}, Massimo Pellizzari ^{3,*} and Alberto Molinari ³

¹ Sandvik Additive Manufacturing, Sandvik Machining Solutions AB, 811 81 Sandviken, Sweden; faraz.deirmina@sandvik.com

² Additive Manufacturing R&D, ProM Facility Area, Trentino Sviluppo S.p.A., Via Fortunato Zeni 8, 38068 Rovereto, Italy; sasan.amir@promfacility.eu

³ Department of Industrial Engineering, University of Trento, Via Sommarive 9, 38123 Trento, Italy; alberto.molinari@unitn.it

* Correspondence: massimo.pellizzari@unitn.it; Tel.: +39-0461-282449

Abstract: Near-full density and crack-free AISI H13 hot-work tool steel was fabricated using laser-directed energy deposition (L-DED). Two different heat-treatment scenarios, i.e., direct tempering (ABT) from the as-built (AB) condition and systematization and quenching prior to tempering (QT), were investigated, and their effect on the microstructure, hardness, fracture toughness (K_{app}), and tempering resistance of the L-DED H13 is reported. For this purpose, the optimal austenitization schedule was identified, and tempering curves were produced. At a similar hardness level (500 HV1), QT parts showed higher K_{app} (89 MPa \sqrt{m}) than ABT (70 MPa \sqrt{m}) levels. However, the fracture toughness values obtained for both parts were comparable to those of wrought H13. The slightly larger K_{app} in the QT counterpart was discussed considering the microstructural homogenization and recrystallization taking place during high-temperature austenitization. The tempering resistance of the ABT material at 600 °C was slightly improved compared with that of the QT material, but for longer holding times (up to 40 h) and higher temperatures (650 °C), ABT showed superior resistance to thermal softening due to a finer martensite substructure (i.e., block size), a finer secondary carbide size, and a larger volume fraction of secondary V(C,N) carbides.

Keywords: additive manufacturing; laser-directed energy deposition; tool steel; heat treatment; hardness; fracture toughness; tempering resistance



Citation: Deirmina, F.; Amirabdollahian, S.; Pellizzari, M.; Molinari, A. Effect of Different Post-Processing Thermal Treatments on the Fracture Toughness and Tempering Resistance of Additively Manufactured H13 Hot-Work Tool Steel. *Metals* **2024**, *14*, 112. <https://doi.org/10.3390/met14010112>

Academic Editor: Namhyun Kang

Received: 15 December 2023

Revised: 4 January 2024

Accepted: 15 January 2024

Published: 17 January 2024



Copyright: © 2024 by the authors. Licensee MDPI, Basel, Switzerland. This article is an open access article distributed under the terms and conditions of the Creative Commons Attribution (CC BY) license (<https://creativecommons.org/licenses/by/4.0/>).

1. Introduction

Additive manufacturing (AM) techniques can considerably improve productivity and decrease the lead time and cost of manufacturing for molds and dies. Moreover, these techniques are able to produce complex geometries and conformal cooling channels that are not achievable using conventional production methods. Laser-directed energy deposition (L-DED) is one of the most practiced laser metal additive manufacturing methods since it provides a unique combination of possibilities, such as the fabrication of large functional parts or prototypes with complex geometries, cladding, repair, and the in situ combination of materials for producing functionally graded materials or alloy designs [1,2].

AISI H13 is a Cr, Mo, V hot-work tool steel that is widely used in tooling applications due to its high hardness and strength, acceptable toughness, and resistance to thermal fatigue and wear at elevated temperatures [3–5]. Despite the difficulties in processing H13 with DED, due to residual stress accumulation resulting from martensitic transformation, numerous studies have been conducted in recent years on the successful deposition and characterization of L-DED H13 parts for tooling applications [6–10]. The as-built (AB) H13 comprises a cellular/dendritic solidification structure, with heavy micro-segregation of

C, and other alloying elements at cellular boundaries, which results in a microstructure comprising a martensitic matrix and considerable amounts (up to ~20 vol.%) of retained austenite (RA) together with a small vol.% of solidification carbides in the intercellular areas [11–13]. Moreover, it has been demonstrated that different thermal histories might lead to an inhomogeneous distribution of phases and microhardness at different locations of the part with respect to the building direction [6,7].

In general, tool steels must be heat-treated to tune their hardness and fracture toughness to meet the service requirements. While conventionally processed tool steels should undergo austenitization and quenching treatments prior to tempering [3], it has been suggested that for AM H13, when experiencing fast cooling after deposition the as-built microstructure can be potentially subjected to direct tempering by the elimination of the costly austenitization step [12–14]. However, few systematic studies have been performed to evaluate the effect of direct tempering on mechanical properties and tempering resistance at elevated temperatures. Deirmina et al. [12,15] compared the effect of two heat-treatment scenarios for laser powder bed fusion-processed H13 and demonstrated that the direct tempering of samples, with the notch perpendicular to the deposited layers, from the as-built condition (ABT) resulted in better static fracture toughness (K_{IC}) compared with the quenched and tempered (QT) counterpart due to the secondary crack formation and crack deflection. On the contrary, for samples with the notch parallel to the deposited layers, the QT counterpart showed significantly higher fracture toughness compared with the ABT counterpart. The latter was also reported by Fonseca et al. [16]. In general, concerning the build direction, the QT samples exhibited less anisotropy in mechanical properties [12,16]. The results of another recent study on a modified H13 grade containing W and higher Mo showed that ABT samples result in better tempering resistance, while the impact toughness was lower than that in QT samples due to the poor microstructural homogeneity in the ABT condition [14].

In the current study, the properties of ABT and QT H13 fabricated by L-DED were investigated to emphasize the main differences. In this regard, tempering resistance and fracture toughness were considered two of the important properties of hot-work tool steels.

2. Materials and Methods

Gas atomized spherical AISI H13 powder (Figure 1a) from Sandvik Osprey, with a particle size distribution (PSD) characterized by a D90 of 109 μm and a D10 of 57 μm (Figure 1b) and a chemical composition (in wt.%) reported in Table 1, were used as feedstock powder.

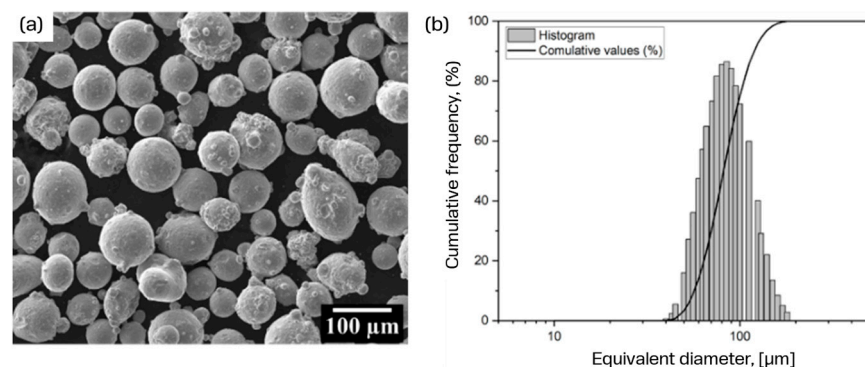


Figure 1. (a) SEM micrograph of feedstock powder, (b) corresponding PSD of the feedstock powder.

Table 1. Chemical composition of the feedstock powder, wt.%.

Element	C	Cr	Mo	Mn	Si	V	N	Fe
	0.40	5.10	1.58	0.30	0.95	1.10	0.04	Bal.

The elements C and N were measured by Leco analysis, and the rest of the elements were quantified using inductively coupled plasma optical emission spectrometry (ICP-OES) in compliance with ISO/IEC 17025:2017 [17].

All the depositions were carried out using a LASERTEC 65 3D hybrid machine (DMG MORI AG, Geretsried, Germany). The machine is equipped with a 2500 W diode laser ($\lambda = 1020$ nm) and a Coax 14 nozzle. The laser has a top-hat beam profile with a spot diameter of 3 mm at a focal length of 13 mm. The machine has a pneumatic powder handling system. Commercially pure Argon was used as both carrier gas and shielding gas with a flow rate of 5 and 5.5 l/min, respectively. An example of processing parameter optimization steps is shown in Figure 2. These steps comprise single-track deposition to select the optimal combination of laser power, powder feed, and scan speed (Figure 2a), followed by single-layer deposition to find the optimal melt pool overlap (Figure 2b), and finally multiple-layer deposition to adjust the layer thickness (Figure 2c). After the process optimization, samples with a relative density of over 99.5% were obtained using printing parameters of $P = 1400$ W, powder flow rate = 12 g/m, and feed rate = 1 m/min using the meander scanning strategy with 90° rotation between layers (Figure 2d). Relative density measurements were conducted using a light optical microscope (LOM), at $50\times$ magnification, on ground and polished metallographic cross-sections, as well as using Archimedes' principle following the standard procedure in ASTM B962 [18]. In this regard, the theoretical density of AISI H13 was assumed to be 7.76 g/cm³.

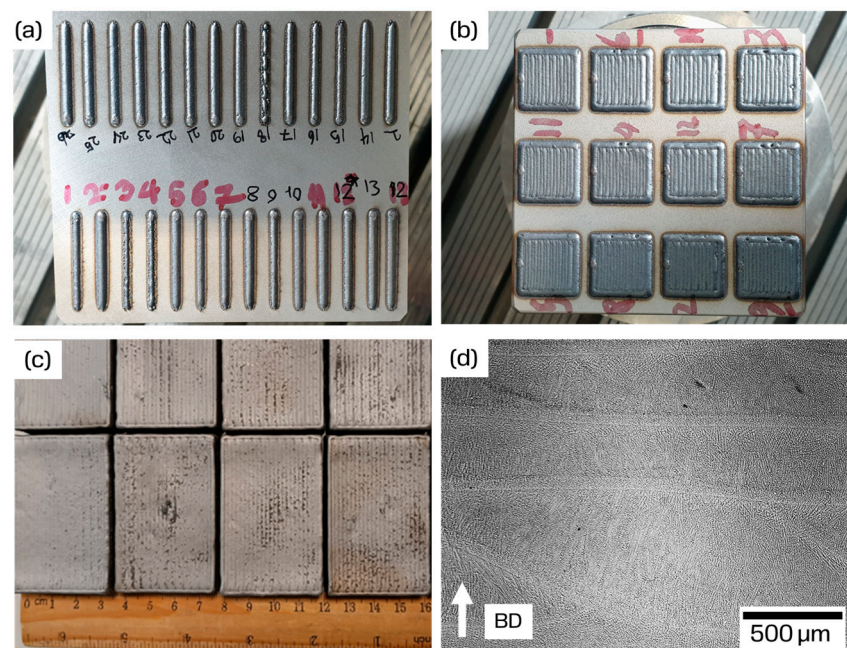


Figure 2. Examples of workflow for L-DED process development. (a) Single-track depositions with laser power, powder feed, and scan speed as variables; (b) single layers with different melt pool overlaps; (c) multiple-layer depositions; and (d) LOM images of the microstructure of samples processed with optimal processing parameters. BD: building direction.

Two different tempering scenarios were selected in a way that obtained a target hardness of ~ 500 HV1 for both QT and ABT samples. In a previous work by the authors, it was demonstrated that 1060 °C can be an optimal austenitization temperature for the L-DED of H13 since it is possible to obtain partial recovery of micro-segregation while avoiding excessive grain growth [12]. In this regard, for QT samples, austenitization at 1060 °C for 45 min was employed, followed by double tempering for 2 h at 600 °C, while ABT counterparts were double-tempered directly from the as-built condition at 625 °C for 2 h. Heat treatments were performed using an L75 Platinum LINSEIS dilatometer in Argon atmosphere. The tempering resistance of the L-DED samples was evaluated by placing

2 sets of QT and ABT samples in a muffle furnace at 600 °C and 650 °C, and hardness measurements were carried out after soaking for 1, 5, 20, and 40 h.

Three single edge notched bend (SENB) specimens ($6 \times 3 \times 30 \text{ mm}^3$) were cut out of the cuboids using wire electro-discharge machining (EDM) for evaluating the fracture toughness for each heat-treatment scenario. Moreover, the notch ($a/w = 0.5$, $\rho = 90 \text{ }\mu\text{m}$) was introduced in the samples by EDM; the notch plane was parallel to the building direction (i.e., perpendicular to the build plate). Three-point bending tests were performed under stroke control at a rate of $0.5 \text{ mm}/\text{min}^{-1}$ using a 1343 Instron machine (Instron, Norwood, MA, USA) equipped with a 5 kN load cell. In plane strain fracture toughness testing, the stress concentration factor decreases with an increasing root radii; therefore, higher stress is needed to meet the “critical stress intensity.” This results in a slightly higher apparent fracture toughness (K_{app}) compared with that of the plane strain fracture toughness (K_{IC}) tested with a fatigue pre-cracked specimen (i.e., $\rho \rightarrow 0$) [15,19]. However, for notch radii below $100 \text{ }\mu\text{m}$, the K_{app} do not appear to vary significantly as a function of notch radii [19].

Vickers hardness measurements using a load of 9.81 N (HV1) were performed on the ground (up to 1200 grit) and polished ($1 \text{ }\mu\text{m}$ finish) cross-sections using an FM310, FU-TURE-TECH CORP., Japan, according to ASTM E92-17. To report the hardness of the samples used for fracture toughness tests, HV10 measurements were carried out. Microstructure characterization was performed on metallographic cross-sections with an LOM using Nital 2% and on unetched specimens by Field Emission Gun Scanning Electron Microscopy (FE-SEM, Zeiss Sigma, Jena, Germany). Electron backscattered diffraction (EBSD) was conducted using a Symmetry EBSD detector on FE-SEM. A 20 kV accelerating voltage, a specimen tilt of 70° , and a working distance of 15 mm were used for the EBSD analysis. Channel 5 suite (Tango mapping) was used for the post-processing of EBSD data for the martensite block size measurements. SEM imaging and electron dispersive X-ray spectroscopy (EDS) analysis were performed using an accelerating voltage of 10 kV (working distance = 8.5 mm). Phase constitution was determined via X-ray diffraction (XRD) analysis using an Italstructures (IPD3000) instrument equipped with a Co $K\alpha$ source ($\lambda = 0.17889 \text{ nm}$).

To understand the far-from-equilibrium, fast-solidification sequence in L-DED processes, modified Scheil solidification simulations (i.e., Scheil with back diffusion in the primary phase) were used. A process cooling rate of $2 \times 10^3 \text{ K/s}$ was considered based on the literature [20,21], and the simulation was conducted using Thermo-calc software (2023a, TCFE v12, MOBFE v7.1).

3. Results

3.1. AB and Quenched Microstructure

According to XRD measurements (Figure 3a), the as-built steel comprised martensite and $\sim 12 \text{ vol.}\%$ RA, chemically stabilized because of the heavy micro-segregation of alloying elements in intercellular regions [11,12,22]. This is clearly shown by the EBSD lower-center foreshatter diode (FSD) mode image and the corresponding phase map in Figure 3b,c, respectively. Quenching reduced the RA to volume fractions below the detection limit of XRD ($<2\%$) (Figure 3a). The presence of softer RA is reflected in the lower hardness of the AB material compared with that of the quenched material (i.e., $650 \pm 47 \text{ HV1}$ vs. $690 \pm 2 \text{ HV1}$).

The microstructures of the AB and quenched samples are presented in back scatter electron (BSE) micrographs in Figure 4. It can be observed that in addition to the RA at the cellular boundaries, these areas are characterized by stringers of V(C,N) carbonitrides, as well as particles of M_6C - (brighter than matrix in BSE micrographs) and M_7C_3 -type carbides according to the previous work of the authors [11] (Figure 4a and Table 2). In the quenched condition, the cellular structure was removed and M_6C and M_7C_3 carbides seem to have been dissolved, while V(C,N) stringers still exist, and some globular V-rich particles also emerged (Figure 4b and Table 2).

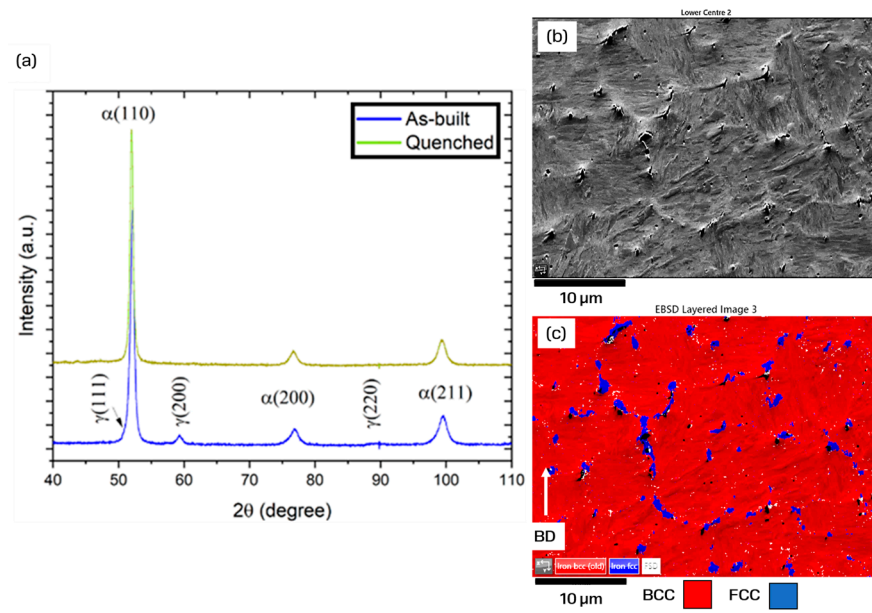


Figure 3. (a) XRD spectra for the AB and quenched L-DED H13, (b) EBSD FSD image showing the matrix and cellular structure in the AB condition, and (c) corresponding EBSD phase map showing the presence of intercellular RA in the AB condition.

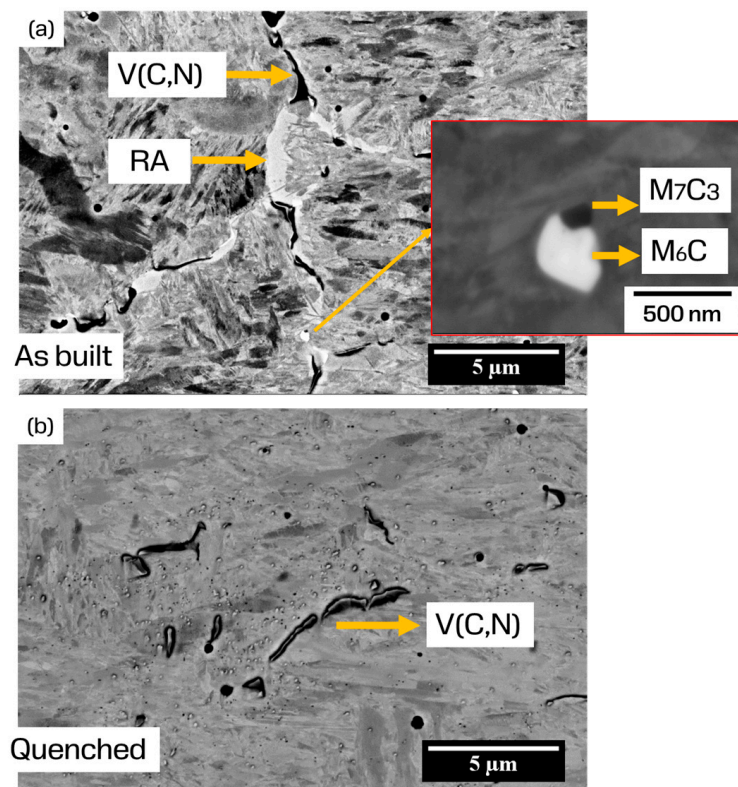


Figure 4. FEG-SEM, BSE micrographs: (a) AB sample with martensitic matrix and cellular solidification structure comprising RA and carbides (inset showing a higher-magnification image of M_6C - M_7C_3 carbides); (b) quenched state with martensitic microstructure and $V(C,N)$ carbonitrides in the form of stringers and newly precipitated globular ones.

Table 2. EDS spot analysis results on carbides in AB and quenched conditions.

Element	AB V(C,N) Stringers	AB (M ₆ C)	AB (M ₇ C ₃)	Quenched V(C,N) Stringers	Quenched V(C,N) Globular
C (at.%)	39.7	26.8	23.3	24.7	22.0
N (wt.%)	4.4	-	-	5.0	1.3
Si (wt.%)	0.6	1.3	-	1.0	0.7
Mn (wt.%)	-	2.5	-	-	-
V (wt.%)	44.0	2.2	5.5	23.1	11.2
Cr (wt.%)	10.5	10.8	25.5	8.3	5.6
Mo (wt.%)	7.7	34.5	8.8	4.3	2.7

The presence of a relatively coarse primary V(C,N) and a finer Mo-rich M₆C adjunct to the Cr-rich M₇C₃ in the as-built microstructure can be explained by modified Scheil simulations (Figure 5a), where the sequence of carbide precipitation from the heavily alloyed remaining liquid during non-equilibrium solidification is as follows:

Liquid → delta ferrite [BCC_A2].

Liquid + delta ferrite → Austenite [FCC_A1].

Liquid → Austenite + V(C,N) [FCCA#2].

Liquid → Austenite + M₆C.

Liquid → Austenite + M₇C₃.

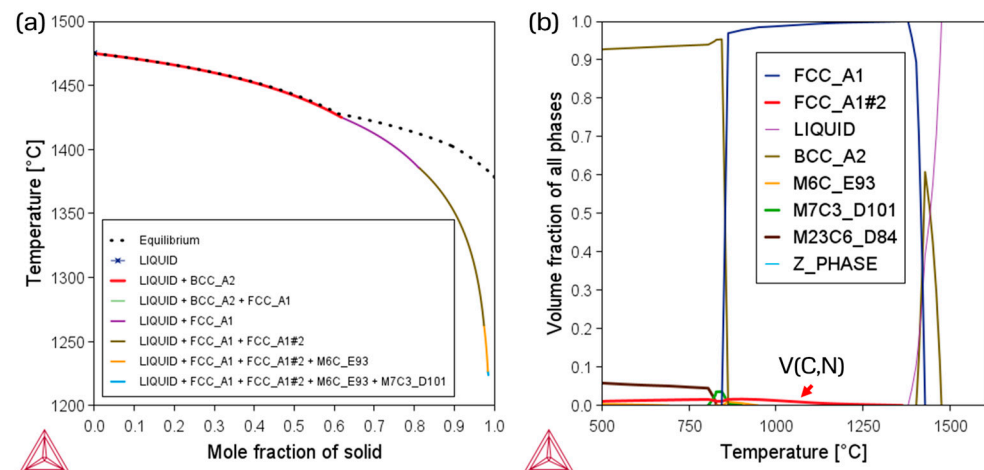


Figure 5. (a) Modified Scheil simulations (with back diffusion in primary phase), where the dashed line is the equilibrium solidification path; and (b) equilibrium step diagrams using the powder chemical composition, where BCC_A2 in the Scheil simulation refers to delta ferrite, while FCC_A1#2 refers to V(C,N) in both figures.

In the quenched state, the dissolution of M₆C and M₇C₃ carbides and the stability of V(C,N) carbonitrides can be explained by an equilibrium step diagram (Figure 5b). It is evident that at the austenitizing temperature (1060 °C), V(C,N) is an equilibrium phase, and its dissolution is not likely, while M₆C and M₇C₃ may dissolve as they are not thermodynamically stable at this temperature. In agreement with this diagram, even more V(C,N) in the form of globular particles precipitated during the austenitization process. Indeed, according to image analysis on SEM micrographs, the vol.% of V(C,N) increased from ~0.30% (AB) to ~0.70% in the quenched condition.

3.2. Tempering Curves

The tempering curves for the L-DED of H13 are presented in Figure 6. It can be observed that at identical tempering temperatures, a systematically higher hardness was obtained for ABT samples, above the secondary hardening peak (~500–525 °C), compared

with the QT condition. Moreover, the secondary hardening peak was shifted to a higher temperature for the ABT condition (525 °C vs. 500 °C). This shift was attributed to the decomposition of RA during the direct tempering process [11–13]. The systematically higher-tempered hardness was discussed in view of the finer martensite substructure and larger supersaturation of martensite in elements C and V in the rapidly solidified AB state compared with that of the austenitized and quenched counterpart, as shown and discussed in Figures 4 and 5. The latter resulted in the precipitation of a larger volume fraction of thermally stable secondary V(C,N) carbides during tempering, thus improving the tempering resistance. A full description can be found in the previous work of the authors [11]. In the temper resistance section (Section 3.3) of this paper, the role of secondary V(C,N) will be discussed in more detail.

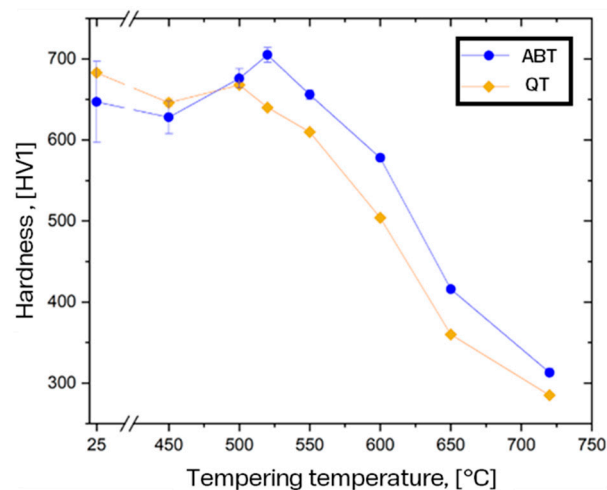


Figure 6. Tempering (2 × 2 h) curves for AB and quenched samples.

Overall, to obtain the same hardness values of 500 HV1 in both samples to perform a meaningful comparison of the fracture toughness and tempering resistance tests, AB samples had to be directly tempered at slightly higher temperatures (+25 °C) compared with the quenched counterparts, i.e., at 625 °C and 600 °C, respectively.

3.3. Tempering Resistance

The over-tempering behavior of the ABT and QT samples at 600 °C and 650 °C is presented in Figure 7. The starting hardness for both conditions was ~520 HV1. At 600 °C, a substantial drop in hardness to 475 HV1 after 5 h was observed for both samples. This is attributed to a drop in the dislocation density of the lath martensite in the initial stages of the test [5]. For longer tempering times, the softening rate decreased for both samples, particularly for ABT. The hardness of ABT decreased to 460 HV1 after 40 h, while that of QT decreased to 425 HV1, confirming the higher tempering resistance after direct tempering from the AB condition. The results of the softening behavior of a wrought hot-work tool steel, initially quenched and tempered followed by soaking at 600 °C, agree well with the behavior of the QT sample in this work (i.e., ~420 HV after 25 h of soaking) [5,23]. Clearly, the improved temper resistance in ABT must be directly correlated to the higher tempering temperature used for ABT (625 °C) than for the QT sample (600 °C) and the higher thermal stability induced.

At 650 °C (i.e., above the initial tempering temperature of both samples), the hardness drop in the early stages of tempering was even more pronounced. After merely 1 h, the hardness declined from 520 HV1 to around 460 HV1 for both samples. At 5 h, the difference in hardness for the ABT and QT samples became more evident. The ABT sample (~425 HV1) showed significantly higher tempering resistance compared with the QT sample (~390 HV1). The hardness difference between the ABT and QT counterparts increased up to 20 h, then remained constant for longer soaking times, i.e., after 40 h the

hardness was 360 HV1 and 300 HV1 for the ABT and QT samples, respectively. Hence, the higher tempering resistance of the ABT counterpart can be confirmed even at a rather high temperature. This is indeed in line with the tempering curves (see Figure 6) showing that the hardness of the ABT sample remained higher compared with that of the QT sample up to temperatures exceeding 700 °C.

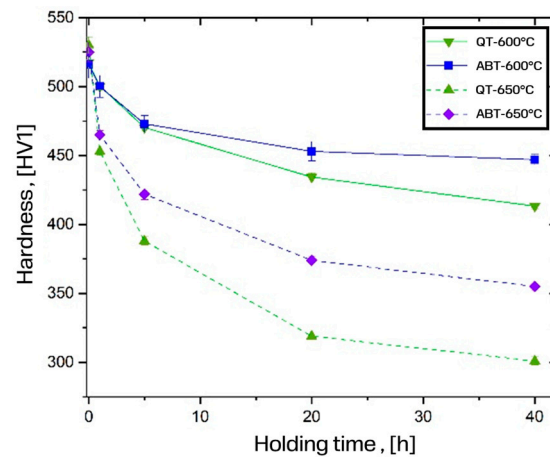


Figure 7. Temper resistance as hardness vs. holding time at 600 °C and 650 °C for ABT and QT samples.

The microstructure of the ABT and QT samples after 40 h of soaking at 650 °C is shown in Figure 8. In ABT, the cellular solidification structures comprising RA and heavily alloyed micro-segregation regions were transformed into a coarse continuous network of carbides precipitated during the high-temperature soaking (over-tempering), in agreement with the previous work of the authors on L-PBF H13, as well as available results in the literature [12–14,24]. The carbide size within the matrix (i.e., inside cells) seemed to be much finer than that of cellular boundary carbides (Figure 8a). On the contrary, the QT sample was characterized by a more uniform carbide distribution because of enhanced microstructural homogenization by the austenitization treatment. The undissolved coarse solidification V(C,N) stringers were still recognizable and are marked with arrows (Figure 8b).

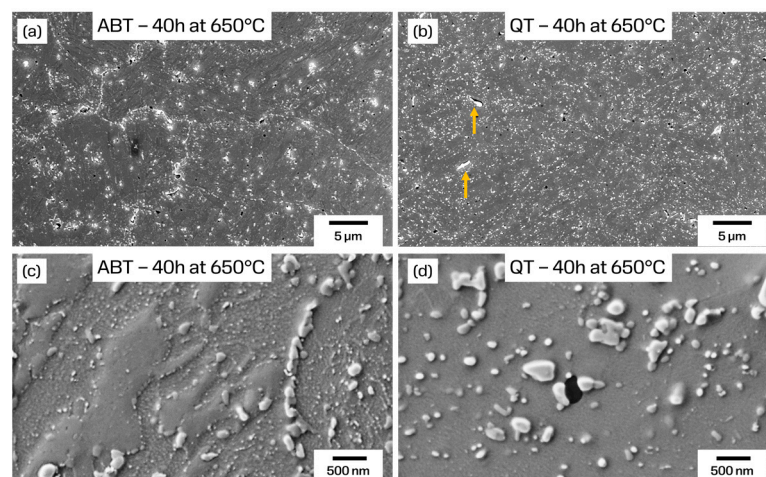


Figure 8. In-Lens SEM micrographs after 40 h of over-tempering at 650 °C. (a) ABT sample showing an interconnected network of carbides precipitated on cellular boundaries, (b) QT sample with more homogenous carbide distribution and presence of undissolved V(C,N) stringers inherited from AB condition, (c) higher-magnification secondary electron image of ABT sample showing extremely fine secondary carbide distribution within martensitic matrix, and (d) higher-magnification secondary electron image of QT sample showing considerably larger secondary carbide sizes.

Higher-magnification images clearly show that within the matrix of the ABT samples, the carbide size is even finer than that of the QT counterpart (Figure 8c,d, respectively). This agrees well with the enhanced over-tempered hardness of the ABT counterpart compared with the QT counterpart, as evident in Figure 7. This is in line with the results on L-PBF H13 reported by Yuan et al. [14], where a finer secondary carbide size was witnessed in the direct tempering scenario compared with the quenched and temper condition at prolonged tempering times.

At higher soaking temperatures (i.e., 650 °C), especially at temperatures higher than the original tempering temperature, the kinetics of dislocation recovery and carbide coarsening are faster. Indeed, the dislocation density drops significantly in the very first hours of tempering [5,14], and the governing softening mechanism in prolonged soaking times is mostly related to the coarsening/transformation of the fine secondary carbides [25]. This depends on the carbide type and initial carbide size.

Martensite substructure boundaries (e.g., lath and block boundaries) are the energetically preferred sites for carbide precipitation. The finer substructure thus provides increased nucleation sites for the carbide precipitation, leading to a finer distribution of carbides and improved temper hardness. This is indeed shown by EBSD band contrast (BC) maps in Figure 9a,b, where the martensite block size is finer in ABT compared with the QT condition (i.e., 310 ± 240 nm vs. 470 ± 340 nm), probably due to the extremely rapid and far-from-equilibrium solidification in the former leading to higher carbon supersaturation in martensite and, thus, a finer block width according to the pioneering work of Morito et al. [26,27], and generally finer grain sizes due to rapid solidification. In these figures, the martensite block boundaries, the smallest subunit in the martensite hierarchy that is characterized by high angle boundaries [28], are marked in blue ($10\text{--}15^\circ$ misorientation angles) and black ($>15^\circ$ misorientation angles). The EBSD results may explain the observations of much finer secondary carbides in the over-tempered ABT sample. Apart from its effect on carbide size, the finer martensite substructure contributes to a higher hardness (strength) through the Hall–Petch relation [28].

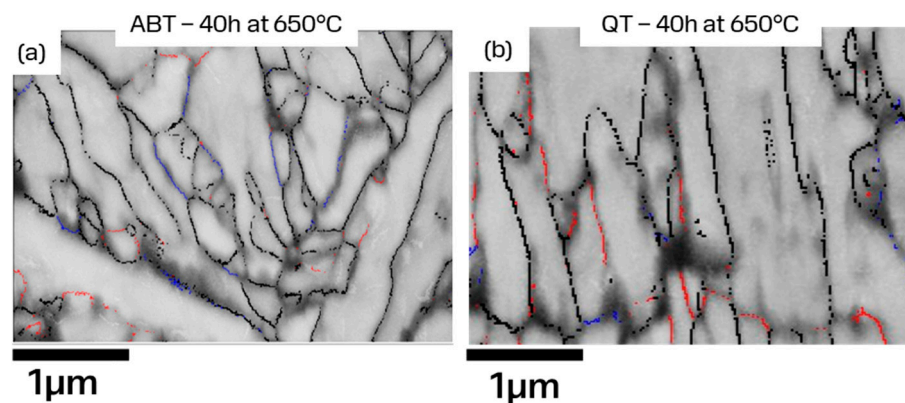


Figure 9. BC maps overlaid by boundaries with misorientation angles of $>2^\circ$ in red, $10\text{--}15^\circ$ in blue, and $>15^\circ$ in black: (a) ABT and (b) QT samples.

The above descriptions might partially explain the enhanced temper resistance of the ABT material.

As a final remark, it has to be mentioned that the role of secondary V(C,N), which is extremely resistant to coarsening, is very significant in terms of thermal softening resistance [5]. As elaborated in Section 3.1., the quenched material contained a larger number of coarse V(C,N) compared with the AB material (i.e., 0.7 vol.% vs. 0.3 vol.%). This was because of the equilibrium precipitation of V(C,N) during the austenitization process (i.e., 1060 °C). This practically reduces the elements C and V in supersaturated solid solutions of quenched martensite compared to AB martensite. Therefore, during the tempering process, a lower number of extremely fine secondary V(C,N) is expected to precipitate within tempered martensite in the QT condition compared with that of the ABT condition.

This will lead to an inferior temper resistance in quenched and tempered material because of the lower vol.% of extremely fine and thermally stable secondary V(C,N).

However, a detailed analysis of the carbide type and size within the martensitic matrix as well as those precipitated on the cellular boundaries is ongoing. The locally higher concentration of alloying elements on the cellular boundaries, due to the micro-segregation, might affect the kinetics of carbide precipitation compared with that in a homogenized material. This is especially true for the micro-segregated elements Mo and V, which show much less mobility compared to Cr, and their segregation might affect the kinetics of carbide precipitation.

3.4. Fracture Toughness

The results of the fracture toughness test are presented in Table 3. It must be again emphasized that the notch root radius ($\sim 90 \mu\text{m}$) in the pre-notched samples realized by EDM was higher than the standard pre-cracked samples ($\rho \rightarrow 0$), which led to a lower stress concentration at the notch tip and an increased plastic zone radius at the crack tip. Therefore, the critical stress intensity factor was generally higher than that measured for a pre-cracked specimen. Consequently, an apparent fracture toughness value (K_{app}) is reported instead of K_{IC} [15,19]. It could be proved that the larger the notch tip radius, the higher K_{app} is than K_{IC} [19]. Therefore, even if the numbers reported in this work can be used to compare the fracture toughness of the ABT and QT conditions, they must be considered overestimated compared with K_{IC} measurements. That being said, the apparent fracture toughness value for the ABT sample ($70 \pm 1.8 \text{ MPa}\sqrt{\text{m}}$) was smaller than that of the QT specimens ($89 \pm 3.8 \text{ MPa}\sqrt{\text{m}}$), but was still comparable to the values obtained using the same method for powder metallurgical (PM) and AM H13 [15,16,29] (see Table 3). For comparison, the K_{IC} values of the wrought products, including electro-slag remelted (ESR) quality H13, tempered to hardness levels close to 500 HV are listed in Table 3.

Table 3. Hardness (HV10) and apparent fracture toughness values for the ABT and QT samples.

Sample	HV10	K_{app} (MPa $\sqrt{\text{m}}$)
AM (L-DED H13-ABT)	495 \pm 5	70 \pm 1.8
AM (L-DED H13-QT)	491 \pm 4	89 \pm 3.8
AM (L-PBF H13-ABT) [15]	460 \pm 5	67.5 \pm 2.8
AM (L-PBF H13-QT) [15]	420 \pm 1	75 \pm 1.0
AM (L-PBF H13-QT) [16]	\sim 550	* $K_{\text{Q}} = 36$
AM (L-PBF H13-QT) [16]	\sim 400	* $K_{\text{Q}} = 84$
HIP H13-QT [29]	450 \pm 10	* $K_{\text{IC}} = 66$
Wrought H13-QT [30]	\sim 530	* $K_{\text{IC}} = 35\text{--}40$
Wrought H13-QT [31]	\sim 470	* $K_{\text{IC}} = 55\text{--}60$

* K_{app} values of this work overestimate the fracture toughness compared to K_{Q} and K_{IC} values reported for AM and wrought steels, respectively.

The crack propagation paths and fracture surfaces are depicted in Figure 10. The crack propagation in ABT was generally trans-granular (Figure 10a). However, crack propagation along the cellular/dendritic boundaries was also evident (shown by arrows). An intercellular fracture was plausible because the cellular boundaries were characterized by a large density of interconnected networks of carbides (see Figure 8a), which were harder than the matrix, where the carbides' coherency with the martensitic matrix was reduced by coarsening through tempering at high temperatures [15]. The dense grain boundary/intercellular precipitation of carbides was the main cause of the lower toughness of the ABT sample compared to the QT sample. Moreover, prior austenite boundaries (PAGs) were elongated parallel to the crack propagation direction in the ABT samples (Figure 10a), whereas in the QT sample with equiaxed PAGs, the result of austenitization treatment, the fracture path seemed to be solely dominated by a trans-granular fracture (Figure 10b).

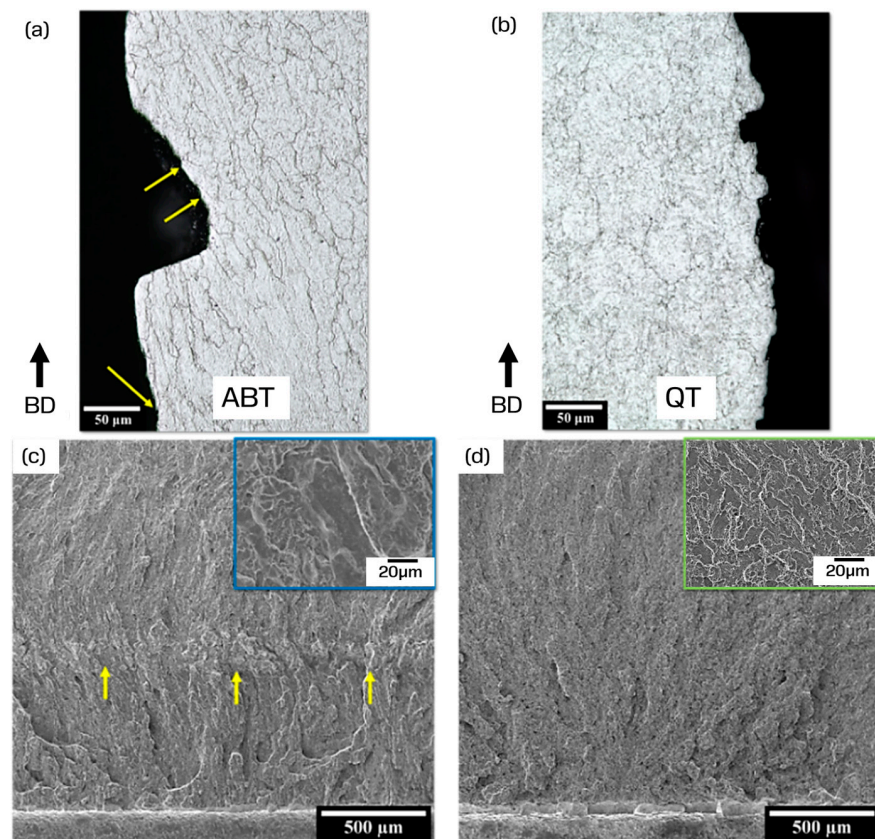


Figure 10. LOM images from fracture paths for (a) ABT and (b) QT samples and relevant SEM micrographs of fracture surfaces in (c) ABT and (d) QT samples; insets show higher-magnification images of fracture surface.

The fracture surface of the ABT samples was governed by cleavage facets with very limited and localized plasticity (see small micro-voids in the inset of Figure 10c). Moreover, traces of the fusion line (melt pool boundaries), caused by the partial remelting between two successive layers, were evident in the ABT samples, and are highlighted by yellow arrows in Figure 10c. This could probably cause a crack deflection as observed in the fracture path images (Figure 10a). In the QT samples, the fracture surface indicated a more quasi-cleavage behavior, with the presence of a larger density and finer distribution of dimples on the fracture surface (see inset in Figure 10d), which is typical in quenched and tempered tool steels [32].

4. Discussion

In industrial practice, tools in H13 experience high temperatures during service. Examples can be hot forging or die casting dies, where for the latter, the casting temperatures can be from ~ 400 °C (Zinc) to ~ 700 °C (Aluminum) and even up to 970 °C (Copper/Brass) [4,5,33–36]. Although for some applications the exposure time can be short, the cumulative effect over a long time during service necessitates the use of materials with improved tempering resistance at elevated temperatures. In this regard, the ABT condition showed outstanding tempering resistance compared with the QT counterpart, as well as compared with wrought H13 [5,23]. On the other hand, it was shown that by austenitization and quenching, a more homogenized microstructure led to enhanced mechanical response in terms of fracture toughness, where austenitization and quenching resulted in enhanced and near-isotropic mechanical properties.

However, given the acceptable fracture toughness measured for ABT and its outstanding tempering resistance, direct tempering may be considered a promising and more cost-effective heat treatment schedule for additively manufactured H13 using laser-based technologies.

This is further confirmed by the improved thermal fatigue resistance of the ABT sample if compared with that of the QT sample based on the most recent work of the authors [37]

5. Conclusions

In the current work, the effect of two different post-processing heat treatments on the properties of the L-DED of H13 hot-work tool steel was investigated. Special emphasis was paid to the fracture toughness and tempering resistance of additively manufactured H13 tool steel after direct tempering (ABT) and quenching and tempering (QT). Based on the results obtained in this work, the following conclusions can be drawn:

- The ABT samples generally demonstrated higher hardness than QT samples tempered at the same temperature. This could be ascribed to the finer martensite substructure leading to higher strength according to the Hall–Petch relation and, at the same time, providing finer secondary carbide size distribution by increased nucleation sites, a plausibly higher volume fraction of thermally stable secondary V(C,N), and, finally, the decomposition of about 12% of the retained austenite during the tempering process.
- The enhanced softening resistance of ABT was extended up to 40 h at 650 °C. Tempering resistance strongly depends on the heat treatment schedule. Direct tempering led to improved tempering resistance due to the contribution of finer martensite substructures and a finer distribution of alloy carbides.
- The QT samples showed higher apparent fracture toughness in comparison to the ABT samples at the same reference hardness (~500 HV1). This was attributed to the more homogeneous micro-structure and the deteriorative effect of densely populated secondary carbides on the cellular/dendritic boundaries in the ABT sample. Nevertheless, the fracture toughness of the ABT samples was still acceptable and comparable to the wrought H13 after heat treatment.

Author Contributions: Conceptualization, F.D., M.P. and A.M.; investigation, S.A. and F.D.; data curation, S.A. and F.D.; writing—original draft preparation, S.A. and F.D.; writing—review and editing, A.M. and M.P. All authors have read and agreed to the published version of the manuscript.

Funding: This research received no external funding.

Data Availability Statement: Data is contained within the article.

Conflicts of Interest: Author Faraz Deirmina was employed by the company Sandvik Machining Solutions AB. The remaining authors declare that the research was conducted in the absence of any commercial or financial relationships that could be construed as a potential conflict of interest.

References

1. Thompson, S.M.; Bian, L.; Shamsaei, N.; Yadollahi, A. An Overview of Direct Laser Deposition for Additive Manufacturing; Part I: Transport Phenomena, Modeling and Diagnostics. *Addit. Manuf.* **2015**, *8*, 36–62. [[CrossRef](#)]
2. Svetlizky, D.; Das, M.; Zheng, B.; Vyatskikh, A.L.; Bose, S.; Bandyopadhyay, A.; Schoenung, J.M.; Lavernia, E.J.; Eliaz, N. Directed Energy Deposition (DED) Additive Manufacturing: Physical Characteristics, Defects, Challenges and Applications. *Mater. Today* **2021**, *49*, 271–295. [[CrossRef](#)]
3. Roberts, G.A.; Kennedy, R.; Krauss, G. *Tool Steels*; ASM International: Detroit, MI, USA, 1998; ISBN 1-61503-201-0.
4. Klobčar, D.; Tušek, J.; Taljat, B. Thermal Fatigue of Materials for Die-Casting Tooling. *Mater. Sci. Eng. A* **2008**, *472*, 198–207. [[CrossRef](#)]
5. Sjöström, J.; Bergström, J. Thermal Fatigue Testing of Chromium Martensitic Hot-Work Tool Steel after Different Austenitizing Treatments. *J. Mater. Process. Technol.* **2004**, *153–154*, 1089–1096. [[CrossRef](#)]
6. Bajaj, P.; Hariharan, A.; Kini, A.; Kürnsteiner, P.; Raabe, D.; Jäggle, E.A. Steels in Additive Manufacturing: A Review of Their Microstructure and Properties. *Mater. Sci. Eng. A* **2020**, *772*, 138633. [[CrossRef](#)]
7. Joshi, S.S.; Sharma, S.; Mazumder, S.; Pantawane, M.V.; Dahotre, N.B. Solidification and Microstructure Evolution in Additively Manufactured H13 Steel via Directed Energy Deposition: Integrated Experimental and Computational Approach. *J. Manuf. Process.* **2021**, *68*, 852–866. [[CrossRef](#)]
8. Park, J.S.; Park, J.H.; Lee, M.-G.; Sung, J.H.; Cha, K.J.; Kim, D.H. Effect of Energy Input on the Characteristic of AISI H13 and D2 Tool Steels Deposited by a Directed Energy Deposition Process. *Metall. Mater. Trans. A* **2016**, *47*, 2529–2535. [[CrossRef](#)]
9. Craig, O.; Bois-Brochu, A.; Plucknett, K. Geometry and Surface Characteristics of H13 Hot-Work Tool Steel Manufactured Using Laser-Directed Energy Deposition. *Int. J. Adv. Manuf. Technol.* **2021**, *116*, 699–718. [[CrossRef](#)]

10. Park, J.S.; Lee, M.-G.; Cho, Y.-J.; Sung, J.H.; Jeong, M.-S.; Lee, S.-K.; Choi, Y.-J.; Kim, D.H. Effect of Heat Treatment on the Characteristics of Tool Steel Deposited by the Directed Energy Deposition Process. *Met. Mater. Int.* **2016**, *22*, 143–147. [[CrossRef](#)]
11. Amirabdollahian, S.; Deirmina, F.; Pellizzari, M.; Bosetti, P.; Molinari, A. Tempering Behavior of a Direct Laser Deposited Hot Work Tool Steel: Influence of Quenching on Secondary Hardening and Microstructure. *Mater. Sci. Eng. A* **2021**, *814*, 141126. [[CrossRef](#)]
12. Deirmina, F.; Peghini, N.; AlMangour, B.; Grzesiak, D.; Pellizzari, M. Heat Treatment and Properties of a Hot Work Tool Steel Fabricated by Additive Manufacturing. *Mater. Sci. Eng. A* **2019**, *753*, 109–121. [[CrossRef](#)]
13. Krell, J.; Röttger, A.; Geenen, K.; Theisen, W. General Investigations on Processing Tool Steel X40CrMoV5-1 with Selective Laser Melting. *J. Mater. Process. Technol.* **2018**, *255*, 679–688. [[CrossRef](#)]
14. Yuan, M.; Cao, Y.; Karamchedu, S.; Hosseini, S.; Yao, Y.; Berglund, J.; Liu, L.; Nyborg, L. Characteristics of a Modified H13 Hot-Work Tool Steel Fabricated by Means of Laser Beam Powder Bed Fusion. *Mater. Sci. Eng. A* **2022**, *831*, 142322. [[CrossRef](#)]
15. Pellizzari, M.; Furlani, S.; Deirmina, F.; Siriki, R.; AlMangour, B.; Grzesiak, D. Fracture Toughness of a Hot Work Tool Steel Fabricated by Laser-Powder Bed Fusion Additive Manufacturing. *Steel Res. Int.* **2020**, *91*, 1900449. [[CrossRef](#)]
16. Fonseca, E.B.; Gabriel, A.H.G.; Ávila, J.A.; Vaz, R.F.; Valim, D.B.; Cano, I.G.; Lopes, É.S.N. Fracture Toughness and Wear Resistance of Heat-Treated H13 Tool Steel Processed by Laser Powder Bed Fusion. *Addit. Manuf.* **2023**, *78*, 103862. [[CrossRef](#)]
17. *ISO/IEC 17025:2017*; General Requirements for the Competence of Testing and Calibration Laboratories. ISO: Geneva, Switzerland, 2017.
18. *ASTM B962*; Standard Test Methods for Density of Compacted or Sintered Powder Metallurgy (PM) Products Using Archimedes' Principle. SIS: London, UK, 2008.
19. Lee, B.-W.; Jang, J.; Kwon, D. Evaluation of Fracture Toughness Using Small Notched Specimens. *Mater. Sci. Eng. A* **2002**, *334*, 207–214. [[CrossRef](#)]
20. König, H.-H.; Pettersson, N.H.; Durga, A.; Van Petegem, S.; Grolimund, D.; Chuang, A.C.; Guo, Q.; Chen, L.; Oikonomou, C.; Zhang, F.; et al. Solidification Modes during Additive Manufacturing of Steel Revealed by High-Speed X-ray Diffraction. *Acta Mater.* **2023**, *246*, 118713. [[CrossRef](#)]
21. Omar, S.M.T.; Plucknett, K.P. The Influence of DED Process Parameters and Heat-Treatment Cycle on the Microstructure and Hardness of AISI D2 Tool Steel. *J. Manuf. Process.* **2022**, *81*, 655–671. [[CrossRef](#)]
22. Chou, C.-Y.; Pettersson, N.H.; Durga, A.; Zhang, F.; Oikonomou, C.; Borgenstam, A.; Odqvist, J.; Lindwall, G. Influence of Solidification Structure on Austenite to Martensite Transformation in Additively Manufactured Hot-Work Tool Steels. *Acta Mater.* **2021**, *215*, 117044. [[CrossRef](#)]
23. Ning, A.; Yue, S.; Gao, R.; Li, L.; Guo, H. Influence of Tempering Time on the Behavior of Large Carbides' Coarsening in AISI H13 Steel. *Metals* **2019**, *9*, 1283. [[CrossRef](#)]
24. Carasi, G.; Yu, B.; Hutten, E.; Zurob, H.; Casati, R.; Vedani, M. Effect of Heat Treatment on Microstructure Evolution of X38CrMoV5-1 Hot-Work Tool Steel Produced by L-PBF. *Metall. Mater. Trans. A* **2021**, *52*, 2564–2575. [[CrossRef](#)]
25. Zhou, Q.; Wu, X.; Shi, N.; Li, J.; Min, N. Microstructure Evolution and Kinetic Analysis of DM Hot-Work Die Steels during Tempering. *Mater. Sci. Eng. A* **2011**, *528*, 5696–5700. [[CrossRef](#)]
26. Morito, S.; Tanaka, H.; Konishi, R.; Furuhashi, T.; Maki, T. The Morphology and Crystallography of Lath Martensite in Fe-C Alloys. *Acta Mater.* **2003**, *51*, 1789–1799. [[CrossRef](#)]
27. Morito, S.; Iwami, Y.; Koyano, T.; Ohba, T. Effect of Solution Carbon and Nitrogen on the Microstructural Size and Crystallography of Lath Martensite in Fe-N and Fe-C Alloys. *Mater. Trans.* **2016**, *57*, 227–232. [[CrossRef](#)]
28. Morito, S.; Yoshida, H.; Maki, T.; Huang, X. Effect of Block Size on the Strength of Lath Martensite in Low Carbon Steels. *Mater. Sci. Eng. A* **2006**, *438–440*, 237–240. [[CrossRef](#)]
29. Pellizzari, M.; Fedrizzi, A.; Zadra, M. Influence of Processing Parameters and Particle Size on the Properties of Hot Work and High Speed Tool Steels by Spark Plasma Sintering. *Mater. Des.* **2011**, *32*, 1796–1805. [[CrossRef](#)]
30. Yuxin, T.; Minghe, L.; Haiyan, C.; Guanghong, Y.; Zhou, X. Effects of Quenching Temperature on Microstructure and Mechanical Properties of H13 Mandrel Steel. *Baosteel Tech. Res.* **2010**, *4*, 58–64.
31. Leskovšek, V. Correlation between the K_{IC}, the H_{RC} and the Charpy V-Notch Test Results for H11/H13 Hot-Work Tool Steels at Room Temperature. *Steel Res. Int.* **2008**, *79*, 306–313. [[CrossRef](#)]
32. Davis, J.R. *ASM Specialty Handbook: Tool Materials*; ASM International: Detroit, MI, USA, 1995; ISBN 0-87170-545-1.
33. Maim, S.; Norström, L.-Å. Material-Related Model for Thermal Fatigue Applied to Tool Steels in Hot-Work Applications. *Met. Sci.* **1979**, *13*, 544–550. [[CrossRef](#)]
34. Hansson, P. Modern Prehardened Tool Steels in Die-Casting Applications. *Mater. Manuf. Process.* **2009**, *24*, 824–827. [[CrossRef](#)]
35. Berns, H.; Wendl, F. Effect of Carbon Content in CrMoV Hot Working Tool Steel. *Steel Res.* **1986**, *57*, 671–676. [[CrossRef](#)]
36. Persson, A.; Hogmark, S.; Bergström, J. Temperature Profiles and Conditions for Thermal Fatigue Cracking in Brass Die Casting Dies. *J. Mater. Process. Technol.* **2004**, *152*, 228–236. [[CrossRef](#)]
37. Pellizzari, M.; Massignani, D.; Amirabdollahian, S.; Deirmina, F. Thermal Fatigue Behavior of AISI H13 Hot Work Tool Steel Produced by Direct Laser Metal Deposition. *Steel Res. Int.* **2023**, *94*, 2200449. [[CrossRef](#)]

Disclaimer/Publisher's Note: The statements, opinions and data contained in all publications are solely those of the individual author(s) and contributor(s) and not of MDPI and/or the editor(s). MDPI and/or the editor(s) disclaim responsibility for any injury to people or property resulting from any ideas, methods, instructions or products referred to in the content.